

The simplest scoto-seesaw model: WIMP dark matter phenomenology and Higgs vacuum stability

Sanjoy Mandal,^{1,*} Rahul Srivastava,^{2,†} and José W. F. Valle^{1,‡}

¹*AHEP Group, Institut de Física Corpuscular –*

CSIC/Universitat de València, Parc Científic de Paterna.

C/ Catedrático José Beltrán, 2 E-46980 Paterna (Valencia) - SPAIN

²*Department of Physics, Indian Institute of Science Education and Research - Bhopal,
Bhopal Bypass Road, Bhauri, Bhopal 462066, India*

We analyze the consistency of electroweak breaking, neutrino and dark matter phenomenology within the simplest scoto-seesaw model. By adding the minimal dark sector to the simplest “missing partner” type-I seesaw one has a physical picture for the neutrino oscillation lengths: the “atmospheric” mass scale arises from the tree-level seesaw, while the “solar” scale is induced radiatively, mediated by the dark sector. We identify parameter regions consistent with theoretical constraints, as well as dark matter relic abundance and direct detection searches. Using two-loop renormalization group equations we explore the stability of the vacuum and the consistency of the underlying dark parity symmetry. One also has a lower bound for the neutrinoless double beta decay amplitude.

1. INTRODUCTION

The discovery of neutrino oscillations [1, 2] implies that at least two neutrinos are massive. There has by now been strong evidence, at different scales, for the existence of cosmological dark matter, the basic understanding and interpretation of which we also lack [3]. The main current neutrino mass generation paradigms are the seesaw and the scotogenic mechanism, which also accounts for dark matter as the mediator of neutrino mass, as a result of an assumed \mathbb{Z}_2 symmetry. Both mechanisms give mass “democratically” to all neutrino states, according to the structure of the relevant Yukawa couplings.

The simplest “scoto-seesaw” extension of the Standard Model [4] combines these two main paradigms within its minimal $SU(3)_c \otimes SU(2)_L \otimes U(1)_Y$ framework. In such hybrid

* smandal@ific.uv.es

† rahul@iiserb.ac.in

‡ valle@ific.uv.es

scenario the atmospheric scale comes from the tree level seesaw, while the solar scale is mediated by the radiative exchange of dark states, i.e.

$$\Delta m_{\text{ATM}}^2 = \left(\frac{v^2}{2M_N} \mathbb{Y}_N^2 \right)^2, \quad \Delta m_{\text{SOL}}^2 \approx \left(\frac{1}{32\pi^2} \right)^2 \left(\frac{\lambda_5 v^2}{M_f^2 - m_\eta^2} M_f \mathbb{Y}_f^2 \right)^2, \quad (1)$$

where M_N is the ‘‘right-handed’’ neutrino mass, M_f and m_η are ‘‘dark-sector’’ masses and \mathbb{Y}_N^2 , \mathbb{Y}_f^2 are corresponding Yukawa coupling strengths.

One sees that the solar splitting will be non-zero as long as $\lambda_5 \neq 0$. Moreover, one accounts naturally for the hierarchy between the solar and atmospheric scales observed in the experimental data [5]. The corresponding ratio of squared solar-to-atmospheric mass splittings for normal and inverted mass hierarchy are found to be [5, 6]:

$$\mathbf{NO}: \frac{\Delta m_{\text{SOL}}^2}{\Delta m_{\text{ATM}}^2} = 0.0294_{-0.0023}^{+0.0027}, \quad \mathbf{IO}: \frac{\Delta m_{\text{SOL}}^2}{\Delta m_{\text{ATM}}^2} = 0.0306_{-0.0025}^{+0.0028}. \quad (2)$$

Altogether, the interplay of the ‘‘seesaw’’ and ‘‘dark-sectors’’ provide an interesting way to describe lepton number violation and neutrino mass generation. Indeed, the scoto-seesaw model has a viable weakly interacting massive particle (WIMP) dark matter candidate and accounts for the observed neutrino masses, including the solar-to-atmospheric hierarchy. The aim of this work is to explore the scoto-seesaw model in more detail.

The paper is organized as follows. In section 2 we briefly describe the model, giving the details of the new fields and their interactions. In section 3, we describe the tree level and radiative neutrino mass generation. In section 4 we study the parameter space for the case of a scalar dark matter candidate. In section 6 we look at vacuum stability in the scoto-seesaw model and show that, over large parameter regions, the vacuum is stable all the way up to the Planck scale. In section 7 we examine the robustness of the dark parity symmetry under renormalization group (RG) evolution of the parameters. We finally conclude in section 8.

2. MINIMAL SCOTO-SEESAW MODEL

The minimal combination of the seesaw mechanism and the scotogenic model was proposed in Ref. [4]¹. It clones the simplest ‘‘missing partner’’ (3,1) version of the Standard Model seesaw mechanism suggested in [8, 9] with the minimal scotogenic model proposed in [10]. We now describe in detail both the fermionic and the scalar sectors of the model.

2.1. The Yukawa Sector

We now briefly recall the basic features of the minimal scoto-seesaw model [4]. The new particles and their charges are given in Table I, where the family index a runs from 1 to 3.

¹ One can have scoto-seesaw realizations based on (3,2) seesaw extensions [7]. While they have new interesting features, one loses the interesting prediction in Eq. (1).

	Standard Model			New Fermions		New Scalar
	L_a	e_a	H	N	f	η
$SU(2)_L$	2	1	2	1	1	2
$U(1)_Y$	-1/2	-1	1/2	0	0	1/2
\mathbb{Z}_2	+	+	+	+	-	-

TABLE I: Matter content and charge assignment of the minimal scoto-seesaw model.

In Table. I the additional \mathbb{Z}_2 symmetry is the “dark parity” responsible for the stability of the dark matter candidate. All the Standard Model particles and N are even under this dark \mathbb{Z}_2 parity, while the dark sector, consisting of one fermion f and one scalar η , is odd under \mathbb{Z}_2 .

The full Yukawa sector can be split as

$$\mathcal{L} = \mathcal{L}_{\text{SM}} + \mathcal{L}_{\text{ATM}} + \mathcal{L}_{\text{DM,SOL}} \quad (3)$$

where \mathcal{L}_{SM} is the Standard Model Lagrangian, while

$$\mathcal{L}_{\text{ATM}} = -Y_N^a \bar{L}^a \tilde{H} N + \frac{1}{2} M_N \bar{N}^c N + h.c., \quad (4)$$

induces the type-I seesaw neutrino mass (atmospheric neutrino mass scale) after the electroweak symmetry breaking. Note also that throughout this work repeated indices imply summation, with $\tilde{H} = i\sigma_2 H^*$, σ_2 being the second Pauli matrix.

The Lagrangian responsible for the solar and dark sector is given by

$$\mathcal{L}_{\text{DM,SOL}} = Y_f^a \bar{L}^a \tilde{\eta} f + \frac{1}{2} M_f \bar{f}^c f + h.c. \quad (5)$$

It induces the solar neutrino mass scale as discussed in Sec. 3.

2.2. The Scalar Sector

Apart from the Standard Model (SM) Higgs doublet H we have a scalar doublet η carrying the same quantum numbers, but with \mathbb{Z}_2 -odd parity. The $SU(3)_c \otimes SU(2)_L \otimes U(1)_Y$ gauge invariant scalar potential is given by

$$V = -\mu_H^2 H^\dagger H + m_\eta^2 \eta^\dagger \eta + \lambda (H^\dagger H)^2 + \lambda_\eta (\eta^\dagger \eta)^2 + \lambda_3 (H^\dagger H) (\eta^\dagger \eta) + \lambda_4 (H^\dagger \eta) (\eta^\dagger H) + \frac{\lambda_5}{2} ((H^\dagger \eta)^2 + h.c.) \quad (6)$$

We now turn to the consistency conditions of the potential. The following restrictions must hold so as to ensure that the scalar potential is bounded from below and has a stable

vacuum at any given energy scale μ :

$$\lambda(\mu) > 0, \quad \lambda_\eta(\mu) > 0, \quad (7)$$

$$\lambda_A \equiv \lambda_3(\mu) + \sqrt{4\lambda(\mu)\lambda_\eta(\mu)} > 0, \quad (8)$$

$$\lambda_B \equiv \lambda_3(\mu) + \lambda_4(\mu) + \sqrt{4\lambda(\mu)\lambda_\eta(\mu)} - |\lambda_5(\mu)| > 0. \quad (9)$$

where $\lambda_i(\mu)$ are the values of the quartic couplings at the running scale μ . In order to have an absolutely stable vacuum, one must satisfy the conditions given in Eqs. (7), (8) and (9) at each and every energy scale. To ensure perturbativity, we take a conservative approach of simply requiring that the scalar quartic couplings in Eq. (6) obey $\leq 4\pi$.

2.3. Mass Spectrum

In order to ensure dark matter stability the \mathbb{Z}_2 symmetry should remain unbroken. This means that the \mathbb{Z}_2 odd scalar η should not acquire a nonzero vacuum expectation value (VEV). As a result, electroweak symmetry breaking is driven simply by the VEV of H . The fields η and H can be expanded as follows

$$H = \begin{pmatrix} H^+ \\ (v + h + i\phi^0)/\sqrt{2} \end{pmatrix}, \quad \eta = \begin{pmatrix} \eta^+ \\ (\eta^R + i\eta^I)/\sqrt{2} \end{pmatrix} \quad (10)$$

Exact conservation of the \mathbb{Z}_2 symmetry forbids the mixing between the Higgs and the dark doublet η . The components of η have the following masses

$$m_{\eta^R}^2 = m_\eta^2 + \frac{1}{2}(\lambda_3 + \lambda_4 + \lambda_5)v^2 \quad (11)$$

$$m_{\eta^I}^2 = m_\eta^2 + \frac{1}{2}(\lambda_3 + \lambda_4 - \lambda_5)v^2 \quad (12)$$

$$m_{\eta^+}^2 = m_\eta^2 + \frac{1}{2}\lambda_3v^2. \quad (13)$$

The difference $m_{\eta^R}^2 - m_{\eta^I}^2$ depends only on the parameter λ_5 which, we will show later, is also responsible for smallness of solar neutrino mass scale. The conservation of the \mathbb{Z}_2 symmetry also makes the lightest of the two eigenstates η^R and η^I a viable scalar dark matter candidate², as we explore in what follows.

² Throughout this work we assume that the dark fermion f is heavier than the dark scalars η^R and η^I .

3. NEUTRINO MASSES

At tree-level this model gives rise to the following neutrino mass matrix \mathcal{M}_ν^{ab} ,

$$\mathcal{M}_\nu^{ab} = \begin{pmatrix} 0 & 0 & 0 & \frac{Y_N^1 v}{\sqrt{2}} \\ 0 & 0 & 0 & \frac{Y_N^2 v}{\sqrt{2}} \\ 0 & 0 & 0 & \frac{Y_N^3 v}{\sqrt{2}} \\ \frac{Y_N^1 v}{\sqrt{2}} & \frac{Y_N^2 v}{\sqrt{2}} & \frac{Y_N^3 v}{\sqrt{2}} & M_N \end{pmatrix} \quad (14)$$

in the basis $(L^a, N)^T$. Notice the (3,1) structure of the seesaw [8, 9], as a result of which one sees that the N pairs off with one combination of the doublets in L_a through their Dirac-like couplings.

This clearly leads to a projective structure for the tree-level neutrino mass matrix

$$\mathcal{M}_{\nu\text{TREE}} = -\frac{v^2}{2M_N} Y_N^a Y_N^b, \quad (15)$$

where $a, b = 1, 2, 3$ are family indices of the lepton doublets. One sees from Eq. (15) that for “sizeable” Yukawa couplings, $Y_N \sim \mathcal{O}(1)$, in order to reproduce the required value of the atmospheric scale, heavy neutrinos must lie at mass scale $M_N \sim \mathcal{O}(10^{14} \text{ GeV})$. Smaller values of the Yukawa coupling Y_N would require correspondingly lower seesaw scale M_N .

The solar mass scale arises from Fig. 1 involving the exchange of the scalar and fermionic dark mediators η and f . Although these corrections also have a projective structure, they

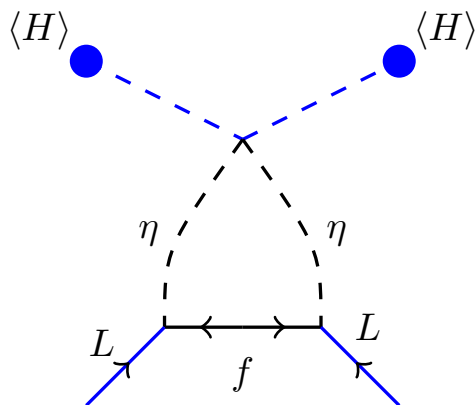


FIG. 1: Solar neutrino mass scale induced from radiative dark-sector exchange.

break the “missing-partner” nature of the (3,1) type-I seesaw mechanism³. The total neutrino mass has the form

$$\mathcal{M}_{\nu\text{TOT}}^{ab} = -\frac{v^2}{2M_N} Y_N^a Y_N^b + \mathcal{F}(m_{\eta R}, m_{\eta I}, M_f) M_f Y_f^a Y_f^b, \quad (16)$$

³ The situation is analogous to neutrino mass generation in bilinear broken R-parity supersymmetry [11–13].

where the first term is the tree-level seesaw part, and the loop function \mathcal{F} characterizes the quantum correction arising from Fig. 1. This is responsible for inducing the solar mass scale.

The loop function \mathcal{F} is expressed as the difference of two B_0 -Veltman functions, namely,

$$\mathcal{F}(m_{\eta^R}, m_{\eta^I}, M_f) = \frac{1}{32\pi^2} \left(\frac{m_{\eta^R}^2 \log(M_f^2/m_{\eta^R}^2)}{M_f^2 - m_{\eta^R}^2} - \frac{m_{\eta^I}^2 \log(M_f^2/m_{\eta^I}^2)}{M_f^2 - m_{\eta^I}^2} \right) \quad (17)$$

Since both terms in Eq. (16) have a projective nature, one out of the three neutrinos remains massless.

From the eigenvalues of the neutrino mass matrix \mathcal{M}_ν^{ab} one can estimate the atmospheric and solar square mass differences as,

$$\Delta m_{\text{ATM}}^2 = \left(\frac{v^2}{2M_N} \mathbb{Y}_N^2 \right)^2, \quad \Delta m_{\text{SOL}}^2 \approx \left(\frac{1}{32\pi^2} \right)^2 \left(\frac{\lambda_5 v^2}{M_f^2 - m_{\eta^R}^2} M_f \mathbb{Y}_f^2 \right)^2. \quad (18)$$

where we take $M_f^2, m_{\eta^R}^2, M_f^2 - m_{\eta^R}^2 \gg \lambda_5 v^2$ and $\mathbb{Y}_\ell^2 = (Y_\ell^e)^2 + (Y_\ell^\mu)^2 + (Y_\ell^\tau)^2$ for $\ell = N, f$. It follows that the ratio between the solar and atmospheric square mass differences can be written as:

$$\frac{\Delta m_{\text{SOL}}^2}{\Delta m_{\text{ATM}}^2} \approx \left(\frac{1}{16\pi^2} \right)^2 \left(\lambda_5 \frac{M_N M_f}{M_f^2 - m_{\eta^R}^2} \right)^2 \left(\frac{\mathbb{Y}_f^2}{\mathbb{Y}_N^2} \right)^2 \quad (19)$$

From Eq. (18) it is clear that one can fit the observed atmospheric and solar mass square differences in many ways as long as one takes an adequately small value for λ_5 . Moreover, Eq. (19) nicely reproduces Eq. (2). In the following we list some choices which can satisfy both the solar and atmospheric scales, as well as have η^R as the scalar WIMP dark matter:

- $M_N \sim 10^{14}$ GeV, $M_f \sim 10^{12}$ GeV, $m_{\eta^R} \sim 10^3$ GeV, $\mathbb{Y}_N \sim 0.4$, $\mathbb{Y}_f \sim 0.4$,
- $M_N \sim 10^{12}$ GeV, $M_f \sim 10^4$ GeV, $m_{\eta^R} \sim 10^3$ GeV, $\mathbb{Y}_N \sim 0.1$, $\mathbb{Y}_f \sim 10^{-4}$,
- $M_N \sim 10^{14}$ GeV, $M_f \sim 10^5$ GeV, $m_{\eta^R} \sim 10^3$ GeV, $\mathbb{Y}_N \sim 0.4$, $\mathbb{Y}_f \sim 10^{-4}$,
- $M_N \sim 10^6$ GeV, $M_f \sim 10^6$ GeV, $m_{\eta^R} \sim 10^3$ GeV, $\mathbb{Y}_N \sim 10^{-5}$, $\mathbb{Y}_f \sim 10^{-4}$.

The upshot of this discussion is that one can easily fit the solar and atmospheric scales for reasonable parameter choices. For example, for sufficiently small λ_5 values, one can choose a reasonable Yukawa coupling \mathbb{Y}_f and $M_f \gtrsim \mathcal{O}(\text{TeV})$. In section 4 we show that either η^I or η^R can, indeed, be taken as a consistent WIMP dark matter candidate.

4. PHENOMENOLOGY OF SCALAR WIMP DARK MATTER

In this section we collect the results of our analysis of dark matter phenomenology. In addition to ensuring radiative generation of neutrino masses, the \mathbb{Z}_2 symmetry in the dark sector ensures the stability of “lightest dark particle” (LDP). Such LDP is in principle a viable dark matter candidate. There are three LDP options. The first is the dark fermion f . The others are the real and imaginary parts of the η scalar, η^R and η^I . In our analysis, we assume scalar dark matter, with the condition $\lambda_5 < 0$ on the quartic coupling λ_5 . As a result η^R will be our dark matter candidate (the opposite scenario with $\lambda_5 > 0$ would have η^I as the dark matter particle).

In order to calculate all the vertices, mass matrices, tadpole equations etc the model is implemented in the SARAH package [14]. On the other hand, the thermal component of the dark matter relic abundance, as well as the dark matter-nucleon scattering cross section, are determined using micrOMEGAS-5.0.8 [15].

4.1. Relic density

As shown in Fig. 9 (Appendix A), there are several dark matter annihilation and coannihilation diagrams present in the scoto-seesaw model. They involve annihilation to quarks and leptons, SM gauge bosons and the Higgs boson. Altogether, they determine the relic abundance of our assumed LDP, η^R . Our numerical scan is performed varying the input parameters as given in Table II.

Parameters	Range
m_η^2	$[100^2, 5000^2] (\text{GeV}^2)$
λ_3	$[10^{-5}, 1]$
λ_4	$[10^{-5}, 1]$
$ \lambda_5 $	$[10^{-5}, 10^{-3}]$

TABLE II: Ranges of variation of the input parameters used in our numerical scan.

In Fig. 2 we show the relic density as a function of the mass of the scalar dark matter candidate η^R . The narrow horizontal band is the 3σ range for cold dark matter derived from the Planck satellite data [16]:

$$0.1126 \leq \Omega_{\eta^R} h^2 \leq 0.1246. \quad (20)$$

Only for solutions falling exactly within this band the totality of the dark matter can be explained by η^R . The relic density for the cyan points in Fig. 2 lies within the above 3σ range, whereas the relic density for blue and gray points is above and below the 3σ range.

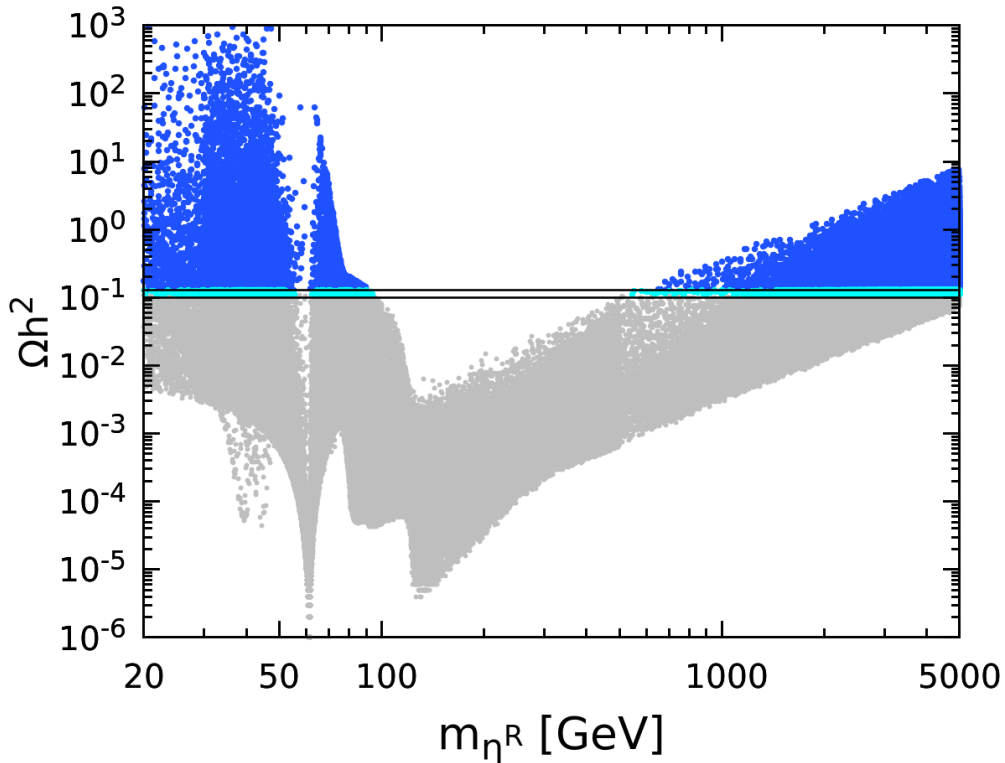


FIG. 2: Relic abundance as a function of the dark matter mass m_{η^R} . Cyan points inside the black lines fall within the measured 3σ cold dark matter relic density range given by Planck satellite data, Eq. (20). Gray (blue) points outside the narrow band give under (over) abundance of dark matter, respectively.

One sees from Fig. 2 that the correct relic density can be obtained in three mass ranges: $m_{\eta^R} < 50$ GeV, 70 GeV $< m_{\eta^R} < 100$ GeV and $m_{\eta^R} > 550$ GeV. The reasons for these mass gaps can be understood by looking in detail into the η^R annihilation channels (see Appendix A). The first dip occurs at $m_{\eta^R} \sim M_Z/2$ and corresponds to annihilation via s-channel Z exchange. The second depletion of the relic density happens around $m_{\eta^R} \sim m_h/2$ and corresponds to annihilations via s-channel Higgs boson exchange. This becomes very efficient when the SM-like Higgs h is on-shell, precluding us from obtaining a relic density matching Planck observations. Notice that the second dip is more efficient than the first one, as the Z -mediated dip is momentum suppressed. For heavier η^R masses, quartic interactions with gauge bosons become effective. For $m_{\eta^R} \gtrsim 80$ GeV, annihilations of η^R into W^+W^- and ZZ via quartic couplings are particularly important, thus explaining the third drop in the relic abundance. In the mass range $m_{\eta^R} \geq 120$ GeV, η^R can annihilate also into two Higgs bosons, hh . When $m_{\eta^R} \geq m_t$, a new channel $\eta^R\eta^R \rightarrow t\bar{t}$ opens up. All these annihilation channels make dark matter annihilation very efficient, and it is difficult to obtain the correct relic density. For very heavy m_{η^R} the relic density increases due to the suppressed annihilation cross section, which drops as $\sim \frac{1}{m_{\eta^R}^2}$. Notice also that the

coannihilation channels with η^I and η^\pm may occur in all regions of the parameter space, with the effect of lowering the relic dark matter density.

4.2. Direct detection

Let us now study the direct detection prospects of our dark matter η^R . In our model, the tree-level spin-independent η^R -nucleon cross section is mediated by the Higgs and the Z portals, see Fig. 3. Notice that, as the η doublet has non-zero hypercharge, the η^R -nucleon

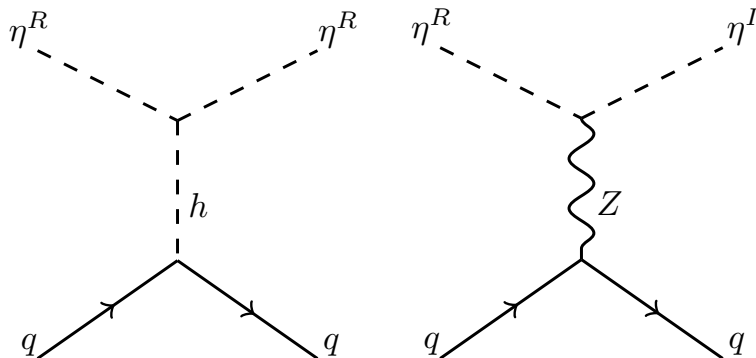


FIG. 3: Higgs and Z -mediated tree-level Feynman diagrams contributing to the elastic scattering of η^R off nuclei.

spin-independent (SI) cross-section is mediated by the Z -boson. Generally this exceeds the current limit from direct detection experiments like XENON1T [17]. However this can be easily avoided by taking non-zero λ_5 . In this case there is a small mass splitting between η^I and η^R , so that the interaction through the Z -boson is kinematically forbidden or leads to inelastic scattering. As a result, for nonzero λ_5 , the η^R -nucleon interaction via the Higgs will be the dominant one. The coupling between η^R and the Higgs boson depends on $\lambda_{345} = \lambda_3 + \lambda_4 + \lambda_5$ and the η^R -nucleon cross section is given by

$$\sigma^{\text{SI}} = \frac{\lambda_{345}^2}{4\pi m_h^4} \frac{m_N^4 f_N^2}{(m_{\eta^R} + m_N)^2} \quad (21)$$

where m_h is the mass of SM Higgs boson and m_N is the nucleon mass, i.e. the average of the proton and neutron masses. Here f_N is the form factor, which depends on hadronic matrix elements. In Fig. 4 we show the spin-independent η^R -nucleon cross section as a function of the η^R mass, for the range of parameters covered by our scan given in Table II. The color code in Fig. 4 is the same as in Fig. 2. The red line denotes the latest upper bound from the XENON1T collaboration. There are constraints from other experiments as well, such as LUX [25] and PandaX-II [26], but weaker when compared to the XENON1T limit. We also show the projected sensitivities for the PandaX-4t [18], LUX-ZEPLIN(LZ) [19],

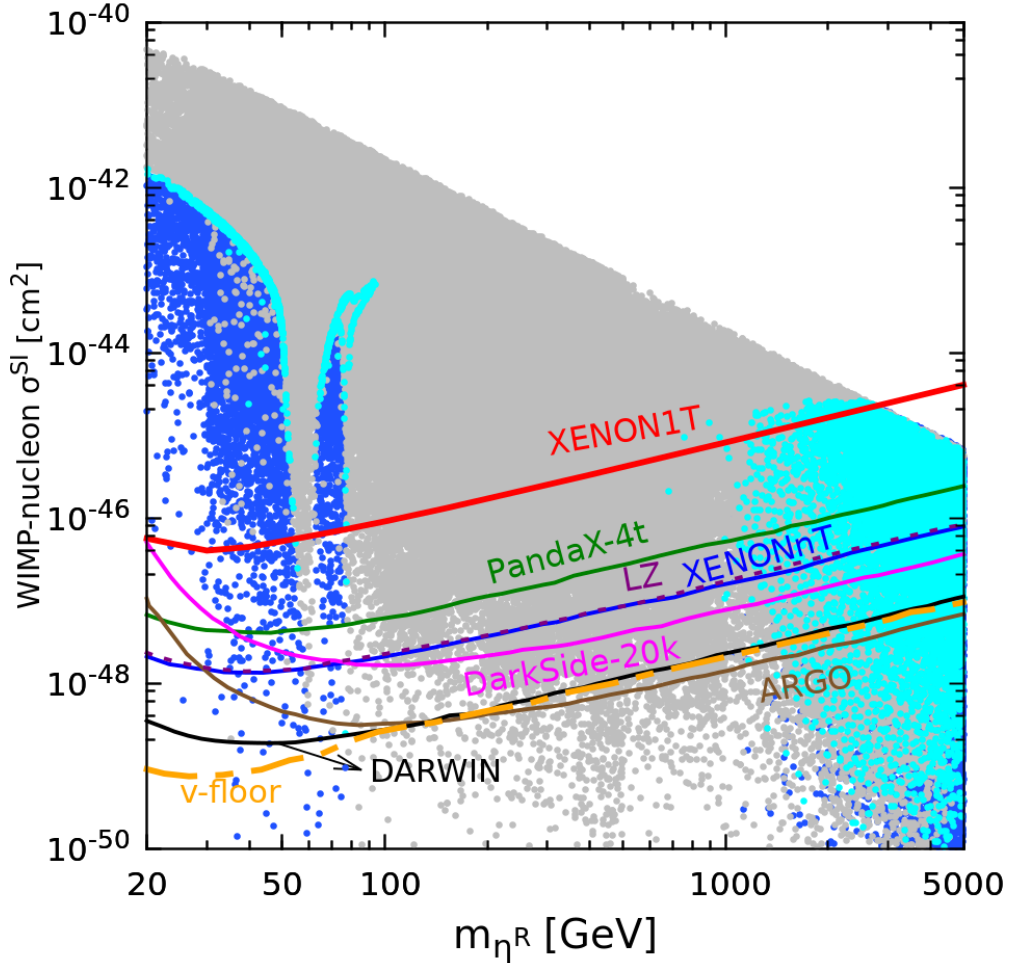


FIG. 4: Spin-independent WIMP-nucleon elastic scattering cross section versus the dark matter mass m_{η^R} , with the same colour code as in Fig. 2. The solid red line denotes the recent upper bound from the XENON1T experiment [17]. A broad region of experimentally viable scoto-seesaw model points in cyan fall within future projected sensitivities for the PandaX-4t [18] (green), LZ [19] (dashed purple), XENONnT with 20 ton-yr exposure [20] (blue), DarkSide-20k [21] (magenta), DARWIN [22] (black) and ARGO [23] (brown) proposals. The dot-dashed orange line corresponds to the “neutrino floor” coming from coherent elastic neutrino scattering [24]. The upper triangular white region violates perturbativity.

XENONnT [20], DarkSide-20k [21], DARWIN [22] and ARGO [23] experiments. The lower limit corresponding to the “neutrino floor” from coherent elastic neutrino scattering is also indicated. We see from Fig. 4 that there are low-mass solutions with the correct dark matter relic density. However, most of these are ruled out by the XENON1T direct detection cross section upper limits. Moreover, there are also tight constraints on low mass dark matter from collider searches, as we will discuss in the next section.

5. COLLIDER CONSTRAINTS

In this section we confront our scalar dark matter candidate η^R with the latest data from particle colliders, in particular the LHC. First we note that, if η^R/η^I are light enough, there are two additional decay channels for the SM-like Higgs boson,

$$\Gamma(h \rightarrow \eta^R \eta^R) = \frac{v^2 \lambda_{345}^2}{32\pi m_h} \sqrt{1 - \frac{4m_{\eta^R}^2}{m_h^2}} \quad (22)$$

$$\Gamma(h \rightarrow \eta^I \eta^I) = \frac{(m_{\eta^I}^2 - m_{\eta^R}^2 + \frac{\lambda_{345}}{2} v^2)^2}{8\pi v^2 m_h} \sqrt{1 - \frac{4m_{\eta^I}^2}{m_h^2}} \quad (23)$$

Note that due to LEP limit $m_{\eta^\pm} > m_W$ [27], there is no phase space for the two body decay $h \rightarrow \eta^\pm \eta^\pm$. The decay mode $\Gamma(h \rightarrow \eta^R \eta^R)$ contributes to the invisible Higgs decay width, constrained by the LHC experiments, e.g. the CMS experiment [28],

$$\text{BR}(h \rightarrow \text{Inv}) \leq 0.19.$$

The SM-like Higgs boson h also couples to the charged Higgs η^\pm , contributing to the diphoton decay channel $h \rightarrow \gamma\gamma$ ⁴. To quantify the deviation from the Standard Model prediction, we define the following parameter

$$R_{\gamma\gamma} = \frac{\text{BR}(h \rightarrow \gamma\gamma)}{\text{BR}(h \rightarrow \gamma\gamma)^{\text{SM}}}. \quad (24)$$

The value we use for the Standard Model is $\text{BR}(h \rightarrow \gamma\gamma)^{\text{SM}} \approx 2.27 \times 10^{-3}$.

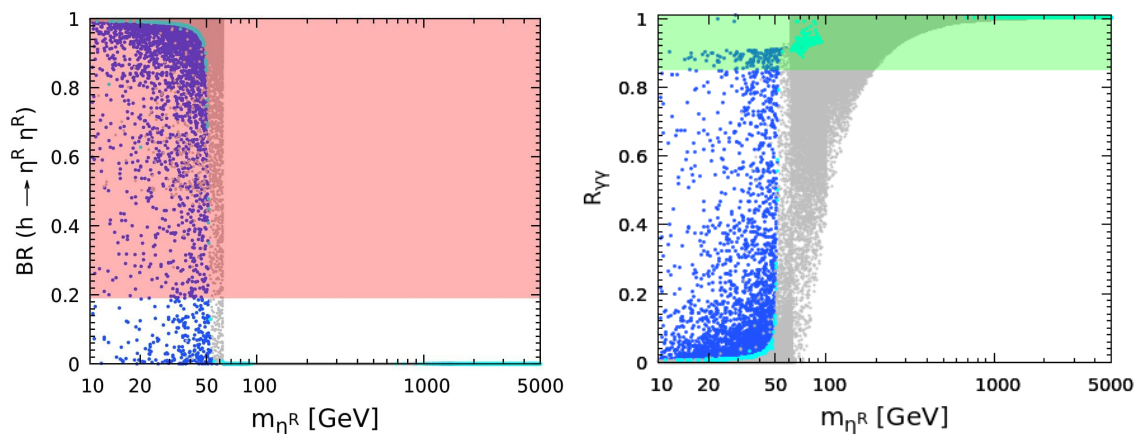


FIG. 5: Invisible Higgs branching ratio (left panel) and $R_{\gamma\gamma}$ (right panel) as a function of the dark matter mass m_{η^R} . The color code is same as in Fig. 2. The shaded red region in the left panel is excluded from the LHC constraint on the invisible Higgs decay [28], while the shaded green band in the right is allowed by ATLAS measurements of $R_{\gamma\gamma}$ [33].

⁴ Note that this invisible Higgs decay and charged scalar contributions to $h \rightarrow \gamma\gamma$ are generic features of inert doublet schemes [29, 30] as well as scotogenic models [31, 32].

The ATLAS and CMS collaborations have studied this decay mode and their combined analysis with 8 TeV data gives $R_{\gamma\gamma}^{\text{exp}} = 1.16_{-0.18}^{+0.20}$ [34]. For the 13 TeV Run-2, there is no combined final data so far, and the available data is separated by production processes [35]. In our analysis we have used 13 TeV ATLAS result which gives the global signal strength measurement of $R_{\gamma\gamma}^{\text{exp}} = 0.99_{-0.14}^{+0.15}$ [33]. In the left panel of Fig. 5 we show the invisible Higgs branching ratio $\text{BR}(h \rightarrow \eta^R \eta^R)$ as a function of the dark matter candidate mass m_{η^R} . In the right panel we give the expected $R_{\gamma\gamma}$ values for the same random scan of parameters. One sees that for low dark matter masses $m_{\eta^R} < 60$ GeV the invisible decay mode $h \rightarrow \eta^R \eta^R$ is open and violates the LHC limit $\text{BR}(h \rightarrow \text{Inv}) \leq 0.19$ [28].

Likewise, the $R_{\gamma\gamma}$ measurement rules out the lower dark matter mass region. For intermediate dark matter masses in the range $70 \text{ GeV} \leq m_{\eta^R} \leq 100 \text{ GeV}$, there are acceptable solutions with acceptable $R_{\gamma\gamma} \approx 1$. In the large mass region $m_{\eta^R} > 550 \text{ GeV}$, the charged Higgs η^\pm contribution to the diphoton decay mode $h \rightarrow \gamma\gamma$ is negligible, so that $R_{\gamma\gamma}$ is close to unity. From the above discussion, one can say that low mass dark matter with $m_{\eta^R} < 60 \text{ GeV}$ is ruled out by LHC constraints. However, they can not completely rule out the intermediate mass region $70 \text{ GeV} \leq m_{\eta^R} \leq 100 \text{ GeV}$. Moreover, the heavy dark matter mass region $m_{\eta^R} > 550 \text{ GeV}$ is completely allowed by LHC constraints.

Before concluding this section we should note that there are also constraints from LEP-I and LEP-II experiments. The precise LEP-I measurements rule out SM-gauge bosons decays to dark sector particles [30, 36]. This requires that

$$m_{\eta^R} + m_{\eta^I}, 2m_{\eta^\pm} > m_Z, \text{ and } m_{\eta^R/\eta^I} + m_{\eta^\pm} > m_W \quad (25)$$

Although there is no dedicated analysis of LEP-II data in the context of scotogenic dark matter models, Ref. [37] has discussed LEP II limits for the case of the Inert Doublet Model, leading to the limits $m_{\eta^R} \gtrsim 80 \text{ GeV}$ and $m_{\eta^I} \gtrsim 100 \text{ GeV}$ and a small $\eta_R - \eta_I$ mass splitting. Altogether, in view of the above, one can say that intermediate dark matter masses in the range $80 \text{ GeV} \leq m_{\eta^R} \leq 100 \text{ GeV}$ are not inconsistent with collider constraints. Dark matter heavier than 550 GeV is perfectly allowed. Dark matter masses in between 100 and 550 GeV could also be possible in the presence of another dark matter component.

6. ELECTROWEAK VACUUM STABILITY

The detailed analysis of the Higgs vacuum within the Standard Model has been carried out in [38–43]. Taking into account the updated input top and Higgs boson mass values one finds that the Standard Model Higgs quartic coupling λ_{SM} becomes negative at $\mu \simeq 10^{10} \text{ GeV}$. This would imply that the Higgs potential is unbounded from below and the Higgs vacuum is unstable. A dedicated analysis shows that, actually, the Standard Model Higgs vacuum is metastable with very long lifetime [43].

Here our aim is to determine the parameter region consistent both with dark matter observations as well as vacuum stability. We first fix the parameters (quartic couplings and mass of the dark matter candidate) which are consistent with the present day relic density and the direct dark matter detection constraints.

In Fig. 6 we have shown the quartic coupling $\lambda_{345} = \lambda_3 + \lambda_4 + \lambda_5$ as a function of dark matter mass m_{η^R} . The color code is same as in Fig. 2. The lower mass region is already

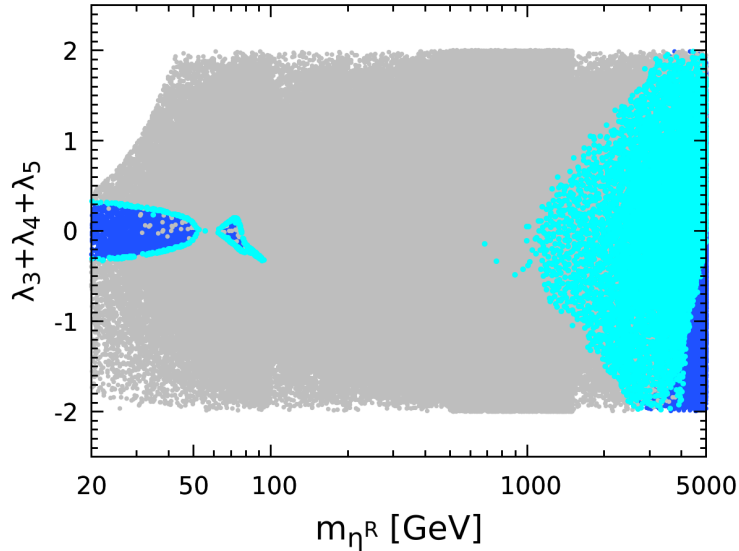


FIG. 6: Coupling $\lambda_{345} = \lambda_3 + \lambda_4 + \lambda_5$ as a function of the dark mass m_{η^R} . The color code is same as in Fig. 2.

excluded by experiment. One sees that in the large mass regime above $m_{\eta^R} > 550$ GeV, the allowed λ_{345} values that successfully explain the relic density while obeying the direct detection limit cover a wide range. For relatively large couplings, the evolution of quartic couplings can make them exceed the perturbativity limit even before the Planck scale. We therefore choose relatively small $\lambda_{3,4,5}$ values. This way λ_{345} is small enough to match the required relic density and to satisfy the direct detection cross section bound for $m_{\eta^R} > 550$ GeV.

We now examine the effect of the new particles present in the scoto-seesaw model upon the stability of the electroweak vacuum. As a “missing partner” (3,1) type-I seesaw cloned with the simplest scotogenic sector, the scoto-seesaw contains the a “right-handed” neutrino N , together with the dark particles f and η . Using SARAH [14] we have computed the two-loop RGEs of the full theory for all the quartic scalar couplings, as well as Yukawa couplings, as given in Appendix B.

We now summarise our results. To begin with, in the effective theory where the heavy singlet fermions N and f are integrated out, we have two natural threshold scales $\Lambda_N \approx M_N$

and $\Lambda_f \approx M_f$. These masses are obtained from Eq. (4) and (5). Hence, in the RGEs of the full theory, we can simply take the Y_N and Y_f Yukawa parameters to be given as $\theta(\mu - M_N)Y_N$, $\theta(\mu - M_f)Y_f$. Clearly they do not run in the effective theory.

Our aim is to study the effect of large as well as small Yukawa couplings on vacuum stability. As discussed before, we take an adequately small but nonzero value for λ_5 , as required for having a reasonable direct detection cross section. For example, with Yukawa couplings $Y_N \sim Y_f \sim \mathcal{O}(1)$ and very large M_N , M_f values, one sees from Eq. (18) that one can easily reproduce the solar and atmospheric scale with $m_{\eta^R} \sim \mathcal{O}(1 \text{ TeV})$.

We now illustrate in more detail the relevant parameter space of the scoto-seesaw model which is consistent with vacuum stability as well as neutrino and dark matter phenomenology. In order to do so we have chosen three sets of benchmarks, given as:

- **BP1:** $M_N \sim 10^{14} \text{ GeV}$, $M_f \sim 10^{12} \text{ GeV}$, $m_{\eta^R} \sim 10^3 \text{ GeV}$, $\mathbb{Y}_N \sim 0.45$, $\mathbb{Y}_f \sim 0.45$,
- **BP2:** $M_N \sim 10^{14} \text{ GeV}$, $M_f \sim 10^5 \text{ GeV}$, $m_{\eta^R} \sim 10^3 \text{ GeV}$, $\mathbb{Y}_N \sim 0.45$, $\mathbb{Y}_f \sim 10^{-4}$,
- **BP3:** $M_N \sim 10^6 \text{ GeV}$, $M_f \sim 10^6 \text{ GeV}$, $m_{\eta^R} \sim 10^3 \text{ GeV}$, $\mathbb{Y}_N \sim 10^{-5}$, $\mathbb{Y}_f \sim 10^{-4}$.

In the upper left, upper right and bottom panel of Fig. 7, we have shown the results for benchmark points **BP1**, **BP2** and **BP3**, respectively. We have taken $\lambda_\eta = 0.1$ and $\lambda = \frac{m_h^2}{2v^2}$ at the electroweak scale. Recall that in order to have an absolutely stable vacuum, one needs to satisfy the conditions given in Eqs. (7), (8) and (9) at all energy scales.

Assuming small λ_5 we show in Fig. 7 the evolution of the remaining four quartic couplings λ , λ_η , λ_A and λ_B . One sees that, with reasonable initial choices, all of the quartic couplings can remain positive and perturbative all the way up to the Planck scale. Since the Yukawa couplings have a negative effect in the RGE evolution of λ , the required value of the quartic couplings λ_3 and λ_4 is correspondingly larger, as seen when going from the upper left to the right panel and finally to the bottom panel in Fig. 7.

To sum up, one sees that the minimal scoto-seesaw model has improved stability properties compared to the type-I seesaw scenario, due to the new scalars needed to realize the scotogenic ‘‘completion’’. The model can explain both solar and atmospheric neutrino mass scales as well as dark matter, upgrading the (3, 1) type-I seesaw mechanism, which can only generate the atmospheric neutrino mass scale. Moreover, the minimal scoto-seesaw model leads to a stable and perturbative electroweak vacuum all the way up to the Planck scale. It can therefore be considered as a full consistent theory for neutrino masses and dark matter.

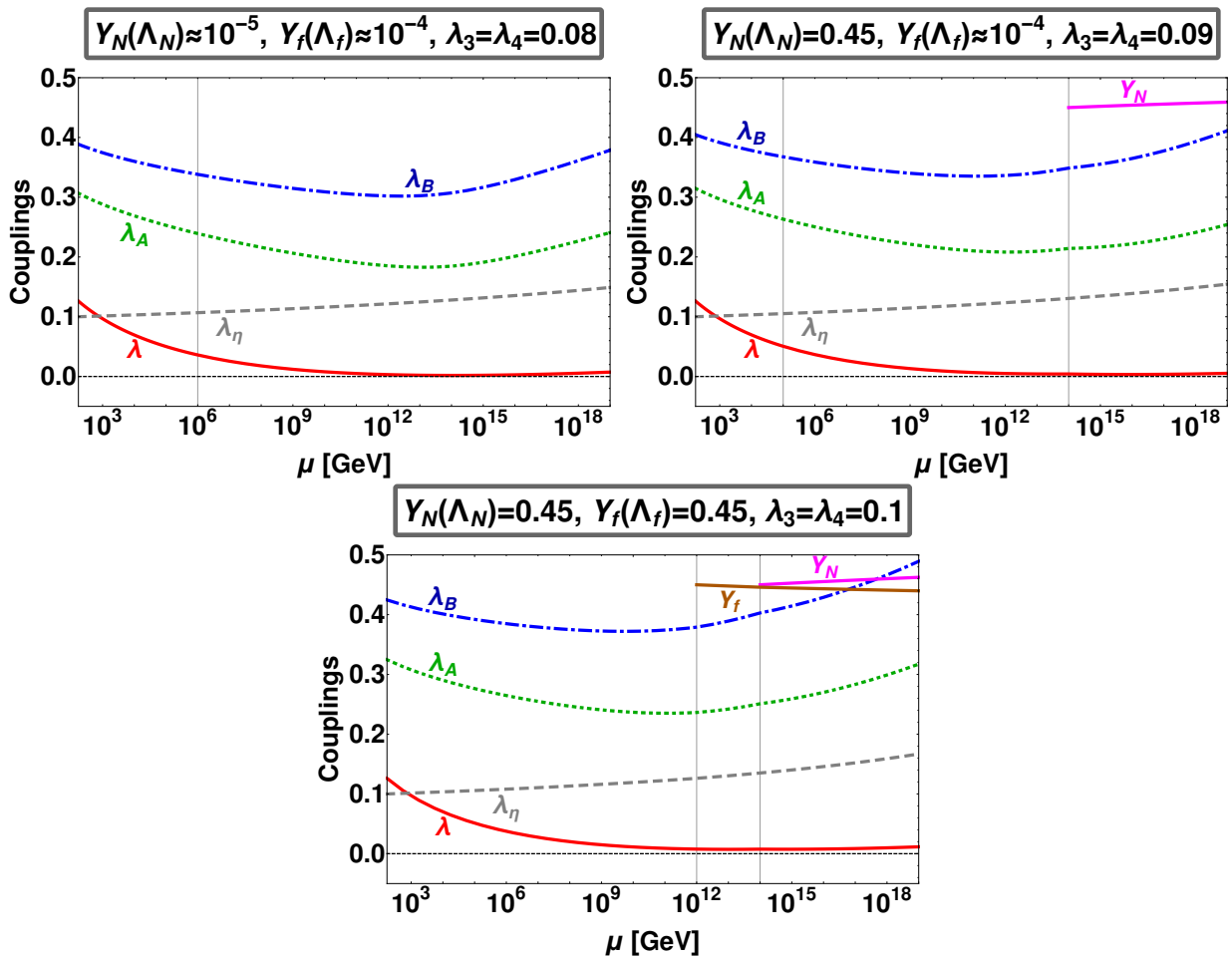


FIG. 7: The RGE-evolution of quartic couplings λ , λ_η , λ_A , λ_B defined in Eqs. (7),(8),(9). The Yukawas Y_N , Y_f are also shown. The values given in the boxes are the initial values at the respective threshold scales. All couplings remain perturbative up to the Planck Scale. Note that we have fixed $m_{\eta_R} = 1$ TeV and taken small $\lambda_5 = 10^{-3}$. See text for more details.

7. HIGH ENERGY BEHAVIOR OF THE DARK PARITY

The conservation of the dark parity is a key feature of the scoto-seesaw model, ensuring dark matter stability as well as the radiative origin of the solar mass scale. Without this \mathbb{Z}_2 symmetry conservation, the LDP would no longer be stable, and also the solar neutrino splitting would not be “calculable” from Eq. (18). It was first pointed out in Ref. [44] that renormalization group evolution can alter the scalar potential at high energies, leading to \mathbb{Z}_2 breaking. It is easy to understand the source of \mathbb{Z}_2 symmetry breaking from the one-loop β function of the m_η^2 parameter. This is given in Appendix B [45, 46]. One needs to focus on the terms which contribute negatively to the evolution of m_η^2 , given in Eq. (B17). We see that with relatively large Yukawa coupling Y_f (i.e. $\lambda_5 \ll 1$) and $M_f^2 > m_\eta^2$, the term $-|M_f|^2|Y_f|^2$ dominates the running of m_η^2 . This can quickly drive m_η^2 towards negative

values and induce a minimum of the scalar potential with $\langle \eta \rangle \neq 0$. Notice, however, that there are terms in Eq. (B17) which can counter this negative effect. For example, terms proportional to the quartic scalar couplings λ_3 and λ_4 may do so if their signs are properly chosen. The contribution to the m_η^2 evolution will be positive for $\lambda_\eta > 0$ and $\lambda_{3,4} < 0$.

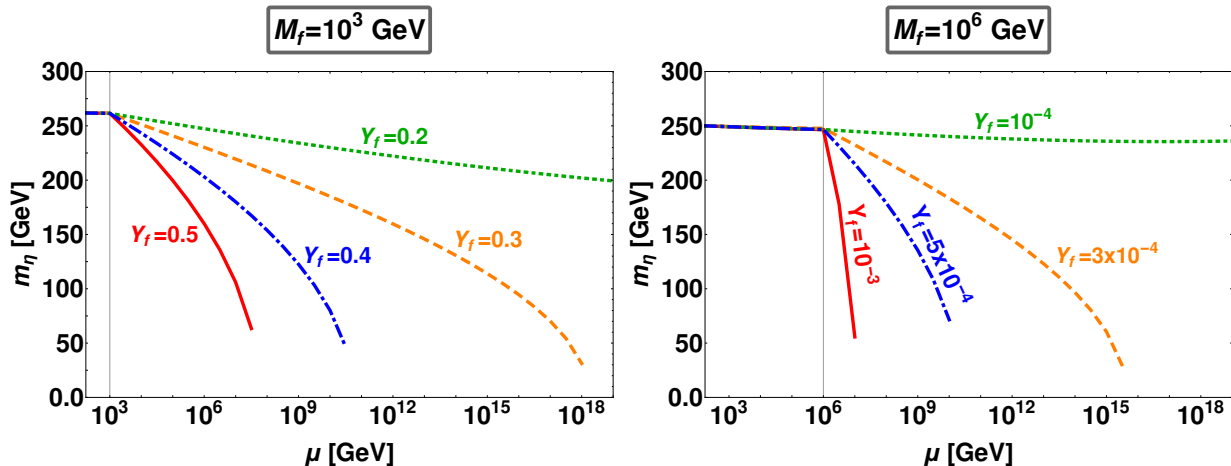


FIG. 8: RGE evolution of m_η as a function of the energy scale μ . For both panels we start running at $m_\eta = 250$ GeV, taking $Y_N = 0$, $\lambda_3 = \lambda_4 = 0.1$ and $\lambda_5 = 10^{-3}$. Different lines correspond to various Yukawa coupling values, as indicated. Note that for $M_f = 10^6$ GeV (right panel) the Yukawas are much smaller. Notice also that all curves terminate when m_η^2 becomes negative (m_η imaginary) indicating \mathbb{Z}_2 breakdown.

Fig. 8 shows the evolution of the scalar mass m_η as a function of energy scale μ . The results have been obtained for two values of M_f , $M_f = 10^3$ GeV (left panel) and 10^6 GeV (right panel). We have fixed $m_\eta^2 = 250^2$ GeV², $\lambda_3 = \lambda_4 = 0.1$, $\lambda_5 \approx 0$ and $Y_N = 0$, for simplicity. The red-solid, blue-dot-dashed, orange-dashed and green-dotted lines in the left (right) panel correspond to four values of the Yukawa coupling Y_f , as indicated. As expected, the \mathbb{Z}_2 breaking scale decreases for larger M_f due to the effect of the term $-|M_f|^2|Y_f|^2$. In other words, the larger the scale M_f , the smaller the allowed value of the Yukawa coupling Y_f in order to have the \mathbb{Z}_2 symmetry preserved all the way up to the Planck scale. From Fig. 8, one sees that the allowed value of this Yukawa coupling is $Y_f \leq 0.2$ for $M_f = 10^3$ GeV, whereas for $M_f = 10^6$ GeV it is $Y_f \leq 10^{-4}$. Although the different quartic couplings such as λ_3 and λ_4 may alter the details, this generic behavior remains. To sum up, we found that in the scoto-seesaw model the dark parity can be preserved up to the Planck scale over large portions of the parameter space.

8. SUMMARY AND DISCUSSION

We have examined the minimal combination of the the seesaw and scotogenic paradigms for neutrino mass generation and dark matter able to “explain” the solar and atmospheric

oscillation wavelengths, in Eqs. 1 and 2. The model provides a simple picture where the “atmospheric” mass scale arises from the tree-level “missing partner” seesaw, while the “solar” scale is induced radiatively by the dark sector, see Fig. 1. We have derived the full two-loop RGEs for the relevant parameters, such as the quartic Higgs self-coupling λ of the Standard Model. The new scalars present in the scoto-seesaw mechanism improve the stability properties of the electroweak vacuum, as seen in Fig. 7. We have also explored the consistency of the underlying dark symmetry, as seen in Fig. 8.

Concerning phenomenology we have discussed scalar dark matter including the experimental restrictions that follow from colliders, Fig. 5. By taking into account the relevant annihilation channels in Fig. 9 we identified viable parameter regions consistent with the required dark matter relic abundance, Fig. 2. Direct dark matter detection by nucleon recoil proceeds through the diagrams in Fig. 3. The expected rates are given in Fig. 4 and offer promising results for upcoming dark matter experiments. We found that the low dark matter mass region $m_{\eta_R} \lesssim 60$ GeV is ruled out by LHC data, but the intermediate region $80 \text{ GeV} \lesssim m_{\eta_R} \lesssim 100$ GeV is still allowed both by LHC and LEP data. The heavier mass region $m_{\eta_R} \gtrsim 550$ GeV is free from collider constraints.

Our construction is very attractive from the point of view of neutrino physics. In contrast to the original scotogenic model where 2 (or 3) species of either dark fermion or dark scalars are needed to generate masses for 2 (or 3) neutrinos, our dark sector is truly minimal, with only one dark fermion and one dark scalar. Therefore, the allowed parameter space differs from the original scotogenic model, though these differences do not translate into a phenomenological smoking-gun signature which can easily distinguish it from canonical scotogenic model in Ref. [10].

Before closing we also note an important phenomenological implication of the minimal scoto-seesaw model that can make it testable. Namely, it implies that one of the neutrinos is massless, as can be readily seen from Eq. (16). This leads to a lower bound on the neutrinoless double beta decay rates even for a normal-ordered neutrino mass spectrum [32, 47–49]. As shown in Fig. 2 of Ref. [32], for an inverted mass spectrum the $0\nu\beta\beta$ lower bound lies substantially higher than in the generic case for that ordering. As a result it falls within the sensitivity of future experiments such as nEXO [50]. In the scoto-seesaw one has that a positive $0\nu\beta\beta$ decay discovery would open bright prospects for the underpinning of the value of the relevant elusive Majorana phase. As discussed in [4], the expected rates for lepton flavour violation processes can also lie within reach of experiments, providing additional signatures. In summary, the scoto-seesaw model is a theoretically consistent and phenomenologically interesting “dark matter completion” of the type-I seesaw mechanism.

ACKNOWLEDGMENTS

This work is supported by the Spanish grant FPA2017-85216-P (AEI/FEDER, UE), PROMETEO/2018/165 (Generalitat Valenciana). R.S. is supported by SERB, Government of India grant SRG/2020/002303.

Appendix A: Scalar dark matter annihilation mechanisms

In the minimal scoto-seesaw model the relic abundance of the lightest dark particle η^R is determined by the following annihilation and coannihilation diagrams.

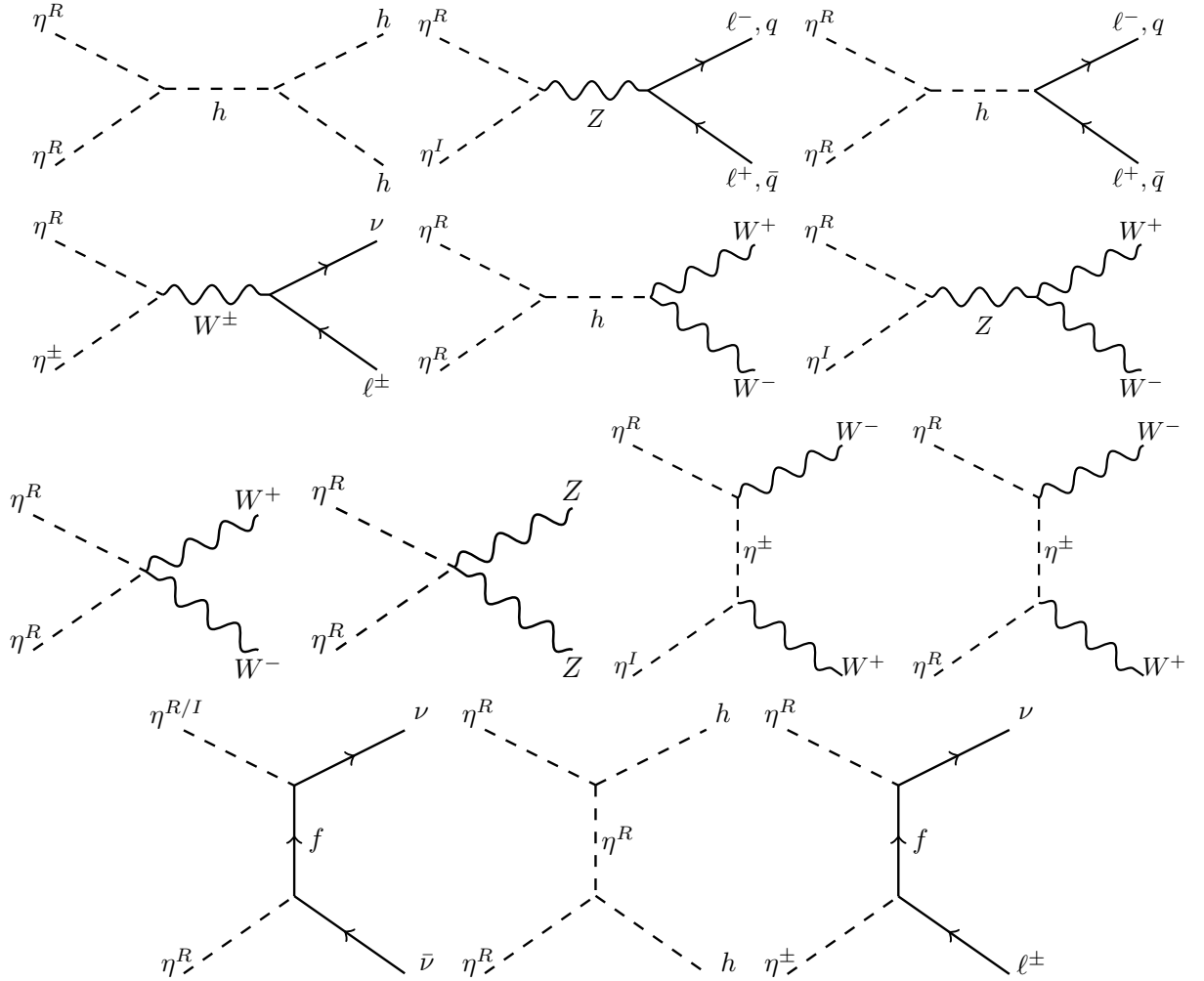


FIG. 9: Annihilation and coannihilation diagrams contributing to the relic abundance of η^R .

Appendix B: Renormalization group equations

The evolution of a given parameter c in the theory is described by the appropriate β function, given by,

$$\frac{dc}{dt} \equiv \beta_c = \frac{1}{16\pi^2}\beta_c^{(1)} + \frac{1}{(16\pi^2)^2}\beta_c^{(2)}.$$

where $\beta_c^{(1)}$ are the one-loop renormalization group (RG) coefficients, while $\beta_c^{(2)}$ correspond to the two-loop RG corrections.

1. Higgs quartic scalar self coupling

The scalar potential of the scoto-seesaw model is given in Eq. (6). The model contains five quartic couplings $\lambda, \lambda_\eta, \lambda_3, \lambda_4, \lambda_5$. The one-loop and two-loop RG equations of the Higgs quartic self-coupling λ are given by

$$\begin{aligned} \beta_\lambda^{(1)} = & +\frac{27}{200}g_1^4 + \frac{9}{20}g_1^2g_2^2 + \frac{9}{8}g_2^4 + 2\lambda_3^2 + 2\lambda_3\lambda_4 + \lambda_4^2 + \lambda_5^2 - \frac{9}{5}g_1^2\lambda - 9g_2^2\lambda + 24\lambda^2 \\ & + 12\lambda y_t^2 + 4\lambda\text{Tr}(Y_N Y_N^\dagger) - 6y_t^4 - 2\text{Tr}(Y_N Y_N^\dagger Y_N Y_N^\dagger), \end{aligned} \quad (\text{B1})$$

$$\begin{aligned} \beta_\lambda^{(2)} = & -\frac{3537}{2000}g_1^6 - \frac{1719}{400}g_1^4g_2^2 - \frac{303}{80}g_1^2g_2^4 + \frac{291}{16}g_2^6 + \frac{9}{10}g_1^4\lambda_3 + \frac{15}{2}g_2^4\lambda_3 + \frac{12}{5}g_1^2\lambda_3^2 + 12g_2^2\lambda_3^2 \\ & - 8\lambda_3^3 + \frac{9}{20}g_1^4\lambda_4 + \frac{3}{2}g_1^2g_2^2\lambda_4 + \frac{15}{4}g_2^4\lambda_4 + \frac{12}{5}g_1^2\lambda_3\lambda_4 + 12g_2^2\lambda_3\lambda_4 - 12\lambda_3^2\lambda_4 + \frac{6}{5}g_1^2\lambda_4^2 \\ & + 3g_2^2\lambda_4^2 - 16\lambda_3\lambda_4^2 - 6\lambda_4^3 - \frac{3}{5}g_1^2\lambda_5^2 - 20\lambda_3\lambda_5^2 - 22\lambda_4\lambda_5^2 + \frac{1953}{200}g_1^4\lambda + \frac{117}{20}g_1^2g_2^2\lambda \\ & - \frac{51}{8}g_2^4\lambda - 20\lambda_3^2\lambda - 20\lambda_3\lambda_4\lambda - 12\lambda_4^2\lambda - 14\lambda_5^2\lambda + \frac{108}{5}g_1^2\lambda^2 + 108g_2^2\lambda^2 - 312\lambda^3 \\ & - 4\lambda_3^2\text{Tr}(Y_f Y_f^\dagger) - 4\lambda_3\lambda_4\text{Tr}(Y_f Y_f^\dagger) - 2\lambda_4^2\text{Tr}(Y_f Y_f^\dagger) - 2\lambda_5^2\text{Tr}(Y_f Y_f^\dagger) - \frac{171}{100}g_1^4y_t^2 \\ & + \frac{63}{10}g_1^2g_2^2y_t^2 - \frac{9}{4}g_2^4y_t^2 + \frac{17}{2}g_1^2\lambda y_t^2 + \frac{45}{2}g_2^2\lambda y_t^2 + 80g_3^2\lambda y_t^2 - 144\lambda^2y_t^2 - \frac{9}{100}g_1^4\text{Tr}(Y_N Y_N^\dagger) \\ & - \frac{3}{10}g_1^2g_2^2\text{Tr}(Y_N Y_N^\dagger) - \frac{3}{4}g_2^4\text{Tr}(Y_N Y_N^\dagger) + \frac{3}{2}g_1^2\lambda\text{Tr}(Y_N Y_N^\dagger) + \frac{15}{2}g_2^2\lambda\text{Tr}(Y_N Y_N^\dagger) \\ & - 48\lambda^2\text{Tr}(Y_N Y_N^\dagger) - 3\lambda\text{Tr}(Y_f Y_f^\dagger Y_N Y_N^\dagger) - \frac{8}{5}g_1^2y_t^4 - 32g_3^2y_t^4 - 3\lambda y_t^4 - \lambda\text{Tr}(Y_N Y_N^\dagger Y_N Y_N^\dagger) \\ & + 30y_t^6 + 2\text{Tr}(Y_f Y_f^\dagger Y_N Y_N^\dagger Y_N Y_N^\dagger) + 10\text{Tr}(Y_N Y_N^\dagger Y_N Y_N^\dagger Y_N Y_N^\dagger). \end{aligned} \quad (\text{B2})$$

$$\begin{aligned} \beta_{\lambda_\eta}^{(1)} = & +\frac{27}{200}g_1^4 + \frac{9}{8}g_2^4 + 2\lambda_3^2 + 2\lambda_3\lambda_4 + \lambda_4^2 + \lambda_5^2 + \frac{9}{20}g_1^2(-4\lambda_\eta + g_2^2) - 9g_2^2\lambda_\eta + 24\lambda_\eta^2 \\ & + 4\lambda_\eta\text{Tr}(Y_f Y_f^\dagger) - 2\text{Tr}(Y_f Y_f^\dagger Y_f Y_f^\dagger) \end{aligned} \quad (\text{B3})$$

$$\begin{aligned}
\beta_{\lambda_\eta}^{(2)} = & -\frac{3537}{2000}g_1^6 - \frac{1719}{400}g_1^4g_2^2 - \frac{303}{80}g_1^2g_2^4 + \frac{291}{16}g_2^6 + \frac{9}{10}g_1^4\lambda_3 + \frac{15}{2}g_2^4\lambda_3 + \frac{12}{5}g_1^2\lambda_3^2 + 12g_2^2\lambda_3^2 \\
& - 8\lambda_3^3 + \frac{9}{20}g_1^4\lambda_4 + \frac{3}{2}g_1^2g_2^2\lambda_4 + \frac{15}{4}g_2^4\lambda_4 + \frac{12}{5}g_1^2\lambda_3\lambda_4 + 12g_2^2\lambda_3\lambda_4 - 12\lambda_3^2\lambda_4 + \frac{6}{5}g_1^2\lambda_4^2 \\
& + 3g_2^2\lambda_4^2 - 16\lambda_3\lambda_4^2 - 6\lambda_4^3 - \frac{3}{5}g_1^2\lambda_5^2 - 20\lambda_3\lambda_5^2 - 22\lambda_4\lambda_5^2 + \frac{1953}{200}g_1^4\lambda_\eta + \frac{117}{20}g_1^2g_2^2\lambda_\eta \\
& - \frac{51}{8}g_2^4\lambda_\eta - 20\lambda_3^2\lambda_\eta - 20\lambda_3\lambda_4\lambda_\eta - 12\lambda_4^2\lambda_\eta - 14\lambda_5^2\lambda_\eta + \frac{108}{5}g_1^2\lambda_\eta^2 + 108g_2^2\lambda_\eta^2 - 312\lambda_\eta^3 \\
& - \lambda_\eta \text{Tr}(Y_f Y_f^\dagger Y_f Y_f^\dagger) + 10\text{Tr}((Y_f Y_f^\dagger Y_f Y_f^\dagger Y_f Y_f^\dagger)) - 3\lambda_\eta \text{Tr}(Y_f Y_N^\dagger Y_N Y_f^\dagger) - 4\lambda_3^2 \text{Tr}(Y_N Y_N^\dagger) \\
& - 4\lambda_3\lambda_4 \text{Tr}(Y_N Y_N^\dagger) - 2\lambda_4^2 \text{Tr}(Y_N Y_N^\dagger) - 2\lambda_5^2 \text{Tr}(Y_N Y_N^\dagger) + \text{Tr}(Y_f Y_f^\dagger) \left(2\text{Tr}(Y_f Y_N^\dagger Y_N Y_f^\dagger) \right) \\
& - \frac{3}{100} \left(10g_1^2 \left(-5\lambda_\eta + g_2^2 \right) + 25 \left(-10g_2^2\lambda_\eta + 64\lambda_\eta^2 + g_2^4 \right) + 3g_1^4 \right) - 12\lambda_3^2 y_t^2 \\
& - 12\lambda_3\lambda_4 y_t^2 - 6\lambda_4^2 y_t^2 - 6\lambda_5^2 y_t^2 \tag{B4}
\end{aligned}$$

$$\begin{aligned}
\beta_{\lambda_4}^{(1)} = & +\frac{9}{5}g_1^2g_2^2 - \frac{9}{5}g_1^2\lambda_4 - 9g_2^2\lambda_4 + 8\lambda_3\lambda_4 + 4\lambda_4^2 + 8\lambda_5^2 + 4\lambda_4\lambda_\eta + 4\lambda_4\lambda + 2\lambda_4 \text{Tr}(Y_f Y_f^\dagger) \\
& - 4\text{Tr}(Y_f Y_N^\dagger Y_N Y_f^\dagger) + 2\lambda_4 \text{Tr}(Y_N Y_N^\dagger) + 6\lambda_4 y_t^2 \tag{B5}
\end{aligned}$$

$$\begin{aligned}
\beta_{\lambda_4}^{(2)} = & -\frac{657}{50}g_1^4g_2^2 - \frac{42}{5}g_1^2g_2^4 + \frac{6}{5}g_1^2g_2^2\lambda_3 + \frac{1413}{200}g_1^4\lambda_4 + \frac{153}{20}g_1^2g_2^2\lambda_4 - \frac{231}{8}g_2^4\lambda_4 + \frac{12}{5}g_1^2\lambda_3\lambda_4 \\
& + 36g_2^2\lambda_3\lambda_4 - 28\lambda_3^2\lambda_4 + \frac{24}{5}g_1^2\lambda_4^2 + 18g_2^2\lambda_4^2 - 28\lambda_3\lambda_4^2 + \frac{48}{5}g_1^2\lambda_5^2 + 54g_2^2\lambda_5^2 - 48\lambda_3\lambda_5^2 \\
& - 26\lambda_4\lambda_5^2 + 6g_1^2g_2^2\lambda_\eta + \frac{24}{5}g_1^2\lambda_4\lambda_\eta - 80\lambda_3\lambda_4\lambda_\eta - 40\lambda_4^2\lambda_\eta - 48\lambda_5^2\lambda_\eta - 28\lambda_4\lambda_\eta^2 + 6g_1^2g_2^2\lambda \\
& + \frac{24}{5}g_1^2\lambda_4\lambda - 80\lambda_3\lambda_4\lambda - 40\lambda_4^2\lambda - 48\lambda_5^2\lambda - 28\lambda_4\lambda^2 - \frac{9}{2}\lambda_4 \text{Tr}(Y_f Y_f^\dagger Y_f Y_f^\dagger) + \text{Tr}(Y_N Y_N^\dagger) \\
& \left(-\frac{3}{5}g_1^2g_2^2 + \frac{3}{4}g_1^2\lambda_4 + \frac{15}{4}g_2^2\lambda_4 - 8\lambda_3\lambda_4 - 4\lambda_4^2 - 8\lambda_5^2 - 8\lambda_4\lambda \right) - \frac{9}{2}\lambda_4 \text{Tr}(Y_N Y_N^\dagger Y_N Y_N^\dagger) \\
& + \text{Tr}(Y_f Y_N^\dagger Y_N Y_f^\dagger) \left(-3\lambda_4 + 8\lambda_3 + 8\text{Tr}(Y_N Y_N^\dagger) \right) + \text{Tr}(Y_f Y_f^\dagger) \left(-\frac{3}{5}g_1^2g_2^2 + \frac{3}{4}g_1^2\lambda_4 \right. \\
& + \frac{15}{4}g_2^2\lambda_4 - 8\lambda_3\lambda_4 - 4\lambda_4^2 - 8\lambda_5^2 - 8\lambda_4\lambda_\eta + 8\text{Tr}(Y_f Y_N^\dagger Y_N Y_f^\dagger) \left. \right) + y_t^2 \left(\frac{63}{5}g_1^2g_2^2 + \frac{17}{4}g_1^2\lambda_4 \right. \\
& \left. + \frac{45}{4}g_2^2\lambda_4 + 40g_3^2\lambda_4 - 24\lambda_3\lambda_4 - 12\lambda_4^2 - 24\lambda_5^2 - 24\lambda_4\lambda - \frac{27}{2}\lambda_4 y_t^2 \right) \tag{B6}
\end{aligned}$$

$$\begin{aligned}
\beta_{\lambda_3}^{(1)} = & +\frac{27}{100}g_1^4 - \frac{9}{10}g_1^2g_2^2 + \frac{9}{4}g_2^4 - \frac{9}{5}g_1^2\lambda_3 - 9g_2^2\lambda_3 + 4\lambda_3^2 + 2\lambda_4^2 + 2\lambda_5^2 + 12\lambda_3\lambda_\eta \\
& + 4\lambda_4\lambda_\eta + 12\lambda_3\lambda + 4\lambda_4\lambda + 2\lambda_3 \text{Tr}(Y_f Y_f^\dagger) + 2\lambda_3 \text{Tr}(Y_N Y_N^\dagger) + 6\lambda_3 y_t^2 \tag{B7}
\end{aligned}$$

$$\begin{aligned}
\beta_{\lambda_3}^{(2)} = & -\frac{3537}{1000}g_1^6 + \frac{909}{200}g_1^4g_2^2 + \frac{33}{40}g_1^2g_2^4 + \frac{291}{8}g_2^6 + \frac{1773}{200}g_1^4\lambda_3 + \frac{33}{20}g_1^2g_2^2\lambda_3 - \frac{111}{8}g_2^4\lambda_3 + \frac{6}{5}g_1^2\lambda_3^2 \\
& + 6g_2^2\lambda_3^2 - 12\lambda_3^3 + \frac{9}{10}g_1^4\lambda_4 - \frac{9}{5}g_1^2g_2^2\lambda_4 + \frac{15}{2}g_2^4\lambda_4 - 12g_2^2\lambda_3\lambda_4 - 4\lambda_3^2\lambda_4 - \frac{6}{5}g_1^2\lambda_4^2 \\
& + 6g_2^2\lambda_4^2 - 16\lambda_3\lambda_4^2 - 12\lambda_4^3 + \frac{12}{5}g_1^2\lambda_5^2 - 18\lambda_3\lambda_5^2 - 44\lambda_4\lambda_5^2 + \frac{27}{10}g_1^4\lambda_\eta - 3g_1^2g_2^2\lambda_\eta \\
& + \frac{45}{2}g_2^4\lambda_\eta + \frac{72}{5}g_1^2\lambda_3\lambda_\eta + 72g_2^2\lambda_3\lambda_\eta - 72\lambda_3^2\lambda_\eta + \frac{24}{5}g_1^2\lambda_4\lambda_\eta + 36g_2^2\lambda_4\lambda_\eta - 32\lambda_3\lambda_4\lambda_\eta \\
& - 28\lambda_4^2\lambda_\eta - 36\lambda_5^2\lambda_\eta - 60\lambda_3\lambda_\eta^2 - 16\lambda_4\lambda_\eta^2 + \frac{27}{10}g_1^4\lambda - 3g_1^2g_2^2\lambda + \frac{45}{2}g_2^4\lambda + \frac{72}{5}g_1^2\lambda_3\lambda \\
& + 72g_2^2\lambda_3\lambda - 72\lambda_3^2\lambda + \frac{24}{5}g_1^2\lambda_4\lambda + 36g_2^2\lambda_4\lambda - 32\lambda_3\lambda_4\lambda - 28\lambda_4^2\lambda - 36\lambda_5^2\lambda - 60\lambda_3\lambda^2 \\
& - 16\lambda_4\lambda^2 - \frac{9}{2}\lambda_3\text{Tr}(Y_fY_f^\dagger Y_fY_f^\dagger) - \frac{9}{100}g_1^4\text{Tr}(Y_NY_N^\dagger) + \frac{3}{10}g_1^2g_2^2\text{Tr}(Y_NY_N^\dagger) - \frac{3}{4}g_2^4\text{Tr}(Y_NY_N^\dagger) \\
& + \frac{3}{4}g_1^2\lambda_3\text{Tr}(Y_NY_N^\dagger) + \frac{15}{4}g_2^2\lambda_3\text{Tr}(Y_NY_N^\dagger) - 4\lambda_3^2\text{Tr}(Y_NY_N^\dagger) - 2\lambda_4^2\text{Tr}(Y_NY_N^\dagger) - 2\lambda_5^2\text{Tr}(Y_NY_N^\dagger) \\
& - 24\lambda_3\lambda\text{Tr}(Y_NY_N^\dagger) - 8\lambda_4\lambda\text{Tr}(Y_NY_N^\dagger) - \frac{9}{2}\lambda_3\text{Tr}(Y_NY_N^\dagger Y_NY_N^\dagger) + \text{Tr}(Y_fY_f^\dagger) \left(-\frac{9}{100}g_1^4 \right. \\
& + \frac{3}{10}g_1^2g_2^2 - \frac{3}{4}g_2^4 + \frac{3}{4}g_1^2\lambda_3 + \frac{15}{4}g_2^2\lambda_3 - 4\lambda_3^2 - 2\lambda_4^2 - 2\lambda_5^2 - 24\lambda_3\lambda_\eta - 8\lambda_4\lambda_\eta + 4\text{Tr}(Y_fY_N^\dagger Y_NY_f^\dagger) \\
& + \text{Tr}(Y_fY_N^\dagger) \left(\text{Tr}(Y_NY_f^\dagger) \left(-3\lambda_3 + 4\text{Tr}(Y_NY_N^\dagger) + 8\lambda_4 \right) \right) + y_t^2 \left(-\frac{171}{100}g_1^4 - \frac{63}{10}g_1^2g_2^2 - \frac{9}{4}g_2^4 \right. \\
& \left. + \frac{17}{4}g_1^2\lambda_3 + \frac{45}{4}g_2^2\lambda_3 + 40g_3^2\lambda_3 - 12\lambda_3^2 - 6\lambda_4^2 - 6\lambda_5^2 - 72\lambda_3\lambda - 24\lambda_4\lambda - \frac{27}{2}\lambda_3y_t^2 \right) \quad (\text{B8})
\end{aligned}$$

$$\begin{aligned}
\beta_{\lambda_5}^{(1)} = & -\frac{9}{5}g_1^2\lambda_5 - 9g_2^2\lambda_5 + 8\lambda_3\lambda_5 + 12\lambda_4\lambda_5 + 4\lambda_5\lambda_\eta + 4\lambda_5\lambda + 2\lambda_5\text{Tr}(Y_fY_f^\dagger) + 2\lambda_5\text{Tr}(Y_NY_N^\dagger) \\
& + 6\lambda_5y_t^2 \quad (\text{B9})
\end{aligned}$$

$$\begin{aligned}
\beta_{\lambda_5}^{(2)} = & +\frac{1413}{200}g_1^4\lambda_5 + \frac{57}{20}g_1^2g_2^2\lambda_5 - \frac{231}{8}g_2^4\lambda_5 + \frac{48}{5}g_1^2\lambda_3\lambda_5 + 36g_2^2\lambda_3\lambda_5 - 28\lambda_3^2\lambda_5 + \frac{72}{5}g_1^2\lambda_4\lambda_5 \\
& + 72g_2^2\lambda_4\lambda_5 - 76\lambda_3\lambda_4\lambda_5 - 32\lambda_4^2\lambda_5 + 6\lambda_5^3 - \frac{12}{5}g_1^2\lambda_5\lambda_\eta - 80\lambda_3\lambda_5\lambda_\eta - 88\lambda_4\lambda_5\lambda_\eta - 28\lambda_5\lambda_\eta^2 \\
& - \frac{12}{5}g_1^2\lambda_5\lambda - 80\lambda_3\lambda_5\lambda - 88\lambda_4\lambda_5\lambda - 28\lambda_5\lambda^2 + \frac{1}{4}\lambda_5 \left(15g_2^2 - 16(2\lambda_3 + 2\lambda_\eta + 3\lambda_4) + 3g_1^2 \right) \text{Tr}(Y_fY_f^\dagger) \\
& - \frac{1}{2}\lambda_5\text{Tr}(Y_fY_f^\dagger Y_fY_f^\dagger) - 3\lambda_5\text{Tr}(Y_fY_N^\dagger Y_NY_f^\dagger) + \frac{3}{4}g_1^2\lambda_5\text{Tr}(Y_NY_N^\dagger) + \frac{15}{4}g_2^2\lambda_5\text{Tr}(Y_NY_N^\dagger) \\
& - 8\lambda_3\lambda_5\text{Tr}(Y_NY_N^\dagger) - 12\lambda_4\lambda_5\text{Tr}(Y_NY_N^\dagger) - 8\lambda_5\lambda\text{Tr}(Y_NY_N^\dagger) - \frac{1}{2}\lambda_5\text{Tr}(Y_NY_N^\dagger Y_NY_N^\dagger) \\
& + y_t^2 \left(\frac{17}{4}g_1^2\lambda_5 + \frac{45}{4}g_2^2\lambda_5 + 40g_3^2\lambda_5 - 24\lambda_3\lambda_5 - 36\lambda_4\lambda_5 - 24\lambda_5\lambda - \frac{3}{2}\lambda_5y_t^2 \right) \quad (\text{B10})
\end{aligned}$$

2. Yukawa Couplings

The one-loop and two-loop RG equations for the Yukawa couplings Y_f , Y_N and y_t are given by

$$\beta_{Y_f}^{(1)} = \frac{1}{20} \left(10 \left(3Y_f Y_f^\dagger Y_f + Y_N Y_N^\dagger Y_f \right) + Y_f \left(20 \text{Tr} \left(Y_f Y_f^\dagger \right) - 9 \left(5g_2^2 + g_1^2 \right) \right) \right), \quad (\text{B11})$$

$$\begin{aligned} \beta_{Y_f}^{(2)} = & + \frac{1}{80} \left(33g_1^2 Y_N Y_N^\dagger Y_f + 165g_2^2 Y_N Y_N^\dagger Y_f - 160\lambda_3 Y_N Y_N^\dagger Y_f - 320\lambda_4 Y_N Y_N^\dagger Y_f \right. \\ & + 120Y_f Y_f^\dagger Y_f Y_f^\dagger Y_f - 20Y_f Y_f^\dagger Y_N Y_N^\dagger Y_f - 20Y_N Y_N^\dagger Y_N Y_N^\dagger Y_f - 180Y_N Y_N^\dagger Y_f y_t^2 \\ & + 3Y_f Y_f^\dagger Y_f \left(225g_2^2 - 320\lambda_\eta - 60 \text{Tr} \left(Y_f Y_f^\dagger \right) + 93g_1^2 \right) + Y_f \left(\frac{117}{200} g_1^4 - \frac{27}{20} g_1^2 g_2^2 \right. \\ & - \frac{21}{4} g_2^4 + \lambda_3^2 + \lambda_3 \lambda_4 + \lambda_4^2 + \frac{3}{2} \lambda_5^2 + 6\lambda_\eta^2 + \frac{3}{8} \left(5g_2^2 + g_1^2 \right) \text{Tr} \left(Y_f Y_f^\dagger \right) \\ & \left. - \frac{9}{4} \text{Tr} \left(Y_f Y_f^\dagger Y_f Y_f^\dagger \right) - \frac{3}{4} \text{Tr} \left(Y_f Y_f^\dagger Y_N Y_N^\dagger \right) \right), \quad (\text{B12}) \end{aligned}$$

$$\beta_{Y_N}^{(1)} = + \frac{1}{2} \left(3Y_N Y_N^\dagger Y_N + Y_f Y_f^\dagger Y_N \right) + Y_N \left(3y_t^2 - \frac{9}{20} g_1^2 - \frac{9}{4} g_2^2 + \text{Tr} \left(Y_N Y_N^\dagger \right) \right), \quad (\text{B13})$$

$$\begin{aligned} \beta_{Y_N}^{(2)} = & + \frac{1}{80} \left(279g_1^2 Y_N Y_N^\dagger Y_N + 675g_2^2 Y_N Y_N^\dagger Y_N - 960\lambda Y_N Y_N^\dagger Y_N - 20Y_f Y_f^\dagger Y_f Y_f^\dagger Y_N \right. \\ & - 20Y_N Y_N^\dagger Y_f Y_f^\dagger Y_N + 120Y_N Y_N^\dagger Y_N Y_N^\dagger Y_N + Y_f Y_f^\dagger Y_N \left(-160\lambda_3 + 165g_2^2 - 320\lambda_4 \right. \\ & + 33g_1^2 - 60 \text{Tr} \left(Y_f Y_f^\dagger \right) \left. \right) - 540Y_N Y_N^\dagger Y_N y_t^2 - 180Y_N Y_N^\dagger Y_N \text{Tr} \left(Y_N Y_N^\dagger \right) \\ & + Y_N \left(\frac{117}{200} g_1^4 - \frac{27}{20} g_1^2 g_2^2 - \frac{21}{4} g_2^4 + \lambda_3^2 + \lambda_3 \lambda_4 + \lambda_4^2 + \frac{3}{2} \lambda_5^2 + 6\lambda^2 + \frac{17}{8} g_1^2 y_t^2 \right. \\ & + \frac{45}{8} g_2^2 y_t^2 + 20g_3^2 y_t^2 + \frac{3}{8} g_1^2 \text{Tr} \left(Y_N Y_N^\dagger \right) + \frac{15}{8} g_2^2 \text{Tr} \left(Y_N Y_N^\dagger \right) - \frac{3}{4} \text{Tr} \left(Y_f Y_f^\dagger Y_N Y_N^\dagger \right) \\ & \left. - \frac{27}{4} y_t^4 - \frac{9}{4} \text{Tr} \left(Y_N Y_N^\dagger Y_N Y_N^\dagger \right) \right), \quad (\text{B14}) \end{aligned}$$

$$\beta_{y_t}^{(1)} = \frac{3}{2} y_t^3 + y_t \left(3y_t^2 - 8g_3^2 - \frac{17}{20} g_1^2 - \frac{9}{4} g_2^2 + \text{Tr} \left(Y_N Y_N^\dagger \right) \right), \quad (\text{B15})$$

$$\begin{aligned} \beta_{y_t}^{(2)} = & + \frac{1}{80} \left(120y_t^5 + y_t^3 \left(1280g_3^2 - 180 \text{Tr} \left(Y_N Y_N^\dagger \right) + 223g_1^2 - 540y_t^2 + 675g_2^2 - 960\lambda \right) \right) \\ & + y_t \left(\frac{1267}{600} g_1^4 - \frac{9}{20} g_1^2 g_2^2 - \frac{21}{4} g_2^4 + \frac{19}{15} g_1^2 g_3^2 + 9g_2^2 g_3^2 - 108g_3^4 + \lambda_3^2 + \lambda_3 \lambda_4 + \lambda_4^2 + \frac{3}{2} \lambda_5^2 \right. \\ & + 6\lambda^2 + \frac{17}{8} g_1^2 y_t^2 + \frac{45}{8} g_2^2 y_t^2 + 20g_3^2 y_t^2 + \frac{3}{8} g_1^2 \text{Tr} \left(Y_N Y_N^\dagger \right) + \frac{15}{8} g_2^2 \text{Tr} \left(Y_N Y_N^\dagger \right) \\ & \left. - \frac{3}{4} \text{Tr} \left(Y_f Y_f^\dagger Y_N Y_N^\dagger \right) - \frac{27}{4} y_t^4 - \frac{9}{4} \text{Tr} \left(Y_N Y_N^\dagger Y_N Y_N^\dagger \right) \right) \quad (\text{B16}) \end{aligned}$$

3. Scalar Mass term

The evolution of the scalar mass-squared term m_η^2 is dictated by the β function

$$\begin{aligned} \beta_{m_\eta^2}^{(1)} = & 12\lambda_\eta m_\eta^2 + 2(-2|M_f|^2 + m_\eta^2) \text{Tr}(Y_f^\dagger Y_f) - 2(\lambda_4 + 2\lambda_3)\mu_H^2 \\ & - \left(\frac{9}{10}g_1^2 + \frac{9}{2}g_2^2\right) m_\eta^2 \end{aligned} \quad (\text{B17})$$

-
- [1] A. B. McDonald, “Nobel Lecture: The Sudbury Neutrino Observatory: Observation of flavor change for solar neutrinos,” *Rev. Mod. Phys.* **88** no. 3, (2016) 030502.
 - [2] T. Kajita, “Nobel Lecture: Discovery of atmospheric neutrino oscillations,” *Rev. Mod. Phys.* **88** no. 3, (2016) 030501.
 - [3] G. Bertone, D. Hooper, and J. Silk, “Particle dark matter: Evidence, candidates and constraints,” *Phys.Rept.* **405** (2005) 279–390.
 - [4] N. Rojas, R. Srivastava, and J. W. F. Valle, “Simplest Scoto-Seesaw Mechanism,” *Phys. Lett.* **B789** (2019) 132–136, [arXiv:1807.11447](https://arxiv.org/abs/1807.11447) [hep-ph].
 - [5] P. F. de Salas *et al.*, “2020 global reassessment of the neutrino oscillation picture,” *JHEP* **02** (2021) 071, [arXiv:2006.11237](https://arxiv.org/abs/2006.11237) [hep-ph].
 - [6] P. F. De Salas *et al.*, “Chi2 profiles from Valencia neutrino global fit.” <http://globalfit.astroparticles.es/>, 2021. <https://doi.org/10.5281/zenodo.4593330>.
 - [7] D. Barreiros, F. Joaquim, R. Srivastava, and J. W. F. Valle, “Minimal scoto-seesaw mechanism with spontaneous CP violation,” [arXiv:2012.05189](https://arxiv.org/abs/2012.05189) [hep-ph].
 - [8] J. Schechter and J. W. F. Valle, “Neutrino Masses in SU(2) x U(1) Theories,” *Phys. Rev.* **D22** (1980) 2227.
 - [9] J. Schechter and J. W. F. Valle, “Neutrino Decay and Spontaneous Violation of Lepton Number,” *Phys. Rev.* **D25** (1982) 774.
 - [10] E. Ma, “Verifiable radiative seesaw mechanism of neutrino mass and dark matter,” *Phys.Rev.* **D73** (2006) 077301, [arXiv:hep-ph/0601225](https://arxiv.org/abs/hep-ph/0601225) [hep-ph].
 - [11] M. Hirsch, M. Diaz, W. Porod, J. Romao, and J. W. F. Valle, “Neutrino masses and mixings from supersymmetry with bilinear R parity violation: A Theory for solar and atmospheric neutrino oscillations,” *Phys.Rev.* **D62** (2000) 113008.
 - [12] M. Diaz *et al.*, “Solar neutrino masses and mixing from bilinear R parity broken supersymmetry: Analytical versus numerical results,” *Phys.Rev.* **D68** (2003) 013009.
 - [13] M. Hirsch and J. W. F. Valle, “Supersymmetric origin of neutrino mass,” *New J.Phys.* **6** (2004) 76.

- [14] F. Staub, “Exploring new models in all detail with SARAH,” *Adv. High Energy Phys.* **2015** (2015) 840780, [arXiv:1503.04200 \[hep-ph\]](#).
- [15] G. Bélanger, F. Boudjema, A. Goudelis, A. Pukhov, and B. Zaldivar, “micrOMEGAs5.0 : Freeze-in,” *Comput. Phys. Commun.* **231** (2018) 173–186, [arXiv:1801.03509 \[hep-ph\]](#).
- [16] **Planck** Collaboration, N. Aghanim *et al.*, “Planck 2018 results. VI. Cosmological parameters,” [arXiv:1807.06209 \[astro-ph.CO\]](#).
- [17] **XENON** Collaboration, E. Aprile *et al.*, “Dark Matter Search Results from a One Ton-Year Exposure of XENON1T,” *Phys. Rev. Lett.* **121** no. 11, (2018) 111302, [arXiv:1805.12562 \[astro-ph.CO\]](#).
- [18] **PandaX** Collaboration, H. Zhang *et al.*, “Dark matter direct search sensitivity of the PandaX-4T experiment,” *Sci. China Phys. Mech. Astron.* **62** no. 3, (2019) 31011, [arXiv:1806.02229 \[physics.ins-det\]](#).
- [19] **LUX-ZEPLIN** Collaboration, D. S. Akerib *et al.*, “Projected WIMP sensitivity of the LUX-ZEPLIN dark matter experiment,” *Phys. Rev. D* **101** no. 5, (2020) 052002, [arXiv:1802.06039 \[astro-ph.IM\]](#).
- [20] **XENON** Collaboration, E. Aprile *et al.*, “Projected WIMP sensitivity of the XENONnT dark matter experiment,” *JCAP* **11** (2020) 031, [arXiv:2007.08796 \[physics.ins-det\]](#).
- [21] **GADMC** Collaboration, C. Galbiati *et al.*, “Future Dark Matter Searches with Low-Radioactivity Argon,” *Input to the European Particle Physics Strategy Update 2018-2020* (2018) . https://indico.cern.ch/event/765096/contributions/3295671/attachments/1785196/2906164/DarkSide-Argo_ESPP_Dec_17_2017.pdf.
- [22] **DARWIN** Collaboration, J. Aalbers *et al.*, “DARWIN: towards the ultimate dark matter detector,” *JCAP* **1611** (2016) 017, [arXiv:1606.07001 \[astro-ph.IM\]](#).
- [23] J. Billard *et al.*, “Direct Detection of Dark Matter – APPEC Committee Report,” [arXiv:2104.07634 \[hep-ex\]](#).
- [24] J. Billard, L. Strigari, and E. Figueroa-Feliciano, “Implication of neutrino backgrounds on the reach of next generation dark matter direct detection experiments,” *Phys. Rev. D* **89** no. 2, (2014) 023524, [arXiv:1307.5458 \[hep-ph\]](#).
- [25] **LUX** Collaboration, D. Akerib *et al.*, “Results from a search for dark matter in the complete LUX exposure,” *Phys.Rev.Lett.* **118** (2017) 021303, [arXiv:1608.07648 \[astro-ph.CO\]](#).
- [26] **PandaX-II** Collaboration, A. Tan *et al.*, “Dark Matter Results from First 98.7 Days of Data from the PandaX-II Experiment,” *Phys. Rev. Lett.* **117** no. 12, (2016) 121303, [arXiv:1607.07400 \[hep-ex\]](#).
- [27] A. Pierce and J. Thaler, “Natural Dark Matter from an Unnatural Higgs Boson and New Colored Particles at the TeV Scale,” *JHEP* **08** (2007) 026, [arXiv:hep-ph/0703056](#).
- [28] **CMS** Collaboration, A. M. Sirunyan *et al.*, “Search for invisible decays of a Higgs boson produced through vector boson fusion in proton-proton collisions at $\sqrt{s} = 13$ TeV,” *Phys.*

- Lett. B* **793** (2019) 520–551, [arXiv:1809.05937 \[hep-ex\]](#).
- [29] R. Barbieri, L. J. Hall, and V. S. Rychkov, “Improved naturalness with a heavy Higgs: An Alternative road to LHC physics,” *Phys. Rev. D* **74** (2006) 015007, [arXiv:hep-ph/0603188](#).
- [30] Q.-H. Cao, E. Ma, and G. Rajasekaran, “Observing the Dark Scalar Doublet and its Impact on the Standard-Model Higgs Boson at Colliders,” *Phys. Rev. D* **76** (2007) 095011, [arXiv:0708.2939 \[hep-ph\]](#).
- [31] C. Bonilla, E. Ma, E. Peinado, and J. W. F. Valle, “Two-loop Dirac neutrino mass and WIMP dark matter,” *Phys.Lett.* **B762** (2016) 214–218, [arXiv:1607.03931 \[hep-ph\]](#).
- [32] I. M. Ávila, V. De Romeri, L. Duarte, and J. W. F. Valle, “Phenomenology of scotogenic scalar dark matter,” *Eur. Phys. J. C* **80** no. 10, (2020) 908, [arXiv:1910.08422 \[hep-ph\]](#).
- [33] **ATLAS** Collaboration, M. Aaboud *et al.*, “Measurements of Higgs boson properties in the diphoton decay channel with 36 fb^{-1} of pp collision data at $\sqrt{s} = 13 \text{ TeV}$ with the ATLAS detector,” *Phys. Rev. D* **98** (2018) 052005, [arXiv:1802.04146 \[hep-ex\]](#).
- [34] **ATLAS, CMS** Collaboration, G. Aad *et al.*, “Measurements of the Higgs boson production and decay rates and constraints on its couplings from a combined ATLAS and CMS analysis of the LHC pp collision data at $\sqrt{s} = 7$ and 8 TeV ,” *JHEP* **08** (2016) 045, [arXiv:1606.02266 \[hep-ex\]](#).
- [35] **ATLAS** Collaboration, G. Aad *et al.*, “Combined measurements of Higgs boson production and decay using up to 80 fb^{-1} of proton-proton collision data at $\sqrt{s} = 13 \text{ TeV}$ collected with the ATLAS experiment,” *Phys. Rev. D* **101** no. 1, (2020) 012002, [arXiv:1909.02845 \[hep-ex\]](#).
- [36] M. Gustafsson, E. Lundstrom, L. Bergstrom, and J. Edsjo, “Significant Gamma Lines from Inert Higgs Dark Matter,” *Phys. Rev. Lett.* **99** (2007) 041301, [arXiv:astro-ph/0703512](#).
- [37] E. Lundstrom, M. Gustafsson, and J. Edsjo, “The Inert Doublet Model and LEP II Limits,” *Phys. Rev. D* **79** (2009) 035013, [arXiv:0810.3924 \[hep-ph\]](#).
- [38] G. Isidori, G. Ridolfi, and A. Strumia, “On the metastability of the standard model vacuum,” *Nucl.Phys.* **B609** (2001) 387–409.
- [39] J. Elias-Miro, J. R. Espinosa, G. F. Giudice, G. Isidori, A. Riotto, and A. Strumia, “Higgs mass implications on the stability of the electroweak vacuum,” *Phys.Lett.* **B709** (2012) 222–228, [arXiv:1112.3022 \[hep-ph\]](#).
- [40] F. Bezrukov, M. Y. Kalmykov, B. A. Kniehl, and M. Shaposhnikov, “Higgs Boson Mass and New Physics,” vol. 1210, p. 140. 2012. [arXiv:1205.2893 \[hep-ph\]](#).
- [41] G. Degrassi *et al.*, “Higgs mass and vacuum stability in the Standard Model at NNLO,” *JHEP* **1208** (2012) 098, [arXiv:1205.6497 \[hep-ph\]](#).
- [42] I. Masina, “Higgs boson and top quark masses as tests of electroweak vacuum stability,” *Phys.Rev.* **D87** (2013) 053001, [arXiv:1209.0393 \[hep-ph\]](#).

- [43] D. Buttazzo, G. Degrassi, P. P. Giardino, G. F. Giudice, F. Sala, A. Salvio, and A. Strumia, “Investigating the near-criticality of the Higgs boson,” *JHEP* **12** (2013) 089, [arXiv:1307.3536 \[hep-ph\]](#).
- [44] A. Merle and M. Platscher, “Parity Problem of the Scotogenic Neutrino Model,” *Phys. Rev. D* **92** no. 9, (2015) 095002, [arXiv:1502.03098 \[hep-ph\]](#).
- [45] A. Merle and M. Platscher, “Running of radiative neutrino masses: the scotogenic model — revisited,” *JHEP* **11** (2015) 148, [arXiv:1507.06314 \[hep-ph\]](#).
- [46] M. Lindner, M. Platscher, C. E. Yaguna, and A. Merle, “Fermionic WIMPs and vacuum stability in the scotogenic model,” *Phys. Rev. D* **94** no. 11, (2016) 115027, [arXiv:1608.00577 \[hep-ph\]](#).
- [47] M. Reig, D. Restrepo, J. W. F. Valle, and O. Zapata, “Bound-state dark matter with Majorana neutrinos,” *Phys.Lett.* **B790** (2019) 303–307, [arXiv:1806.09977 \[hep-ph\]](#).
- [48] D. Barreiros, R. Felipe, and F. Joaquim, “Combining texture zeros with a remnant CP symmetry in the minimal type-I seesaw,” *JHEP* **1901** (2019) 223, [arXiv:1810.05454 \[hep-ph\]](#).
- [49] J. Leite *et al.*, “A theory for scotogenic dark matter stabilised by residual gauge symmetry,” [arXiv:1909.06386 \[hep-ph\]](#).
- [50] M. J. Jewell, *Search for neutrinoless double beta decay with EXO-200 and nEXO*. PhD thesis, Stanford U., 2020. https://stacks.stanford.edu/file/druid:kf548hj0975/jewell_thesis_final_5_1_2020-augmented.pdf.